

Flame-induced pressure gradients in turbulent premixed natural gas-air and hydrogen-air jet flames

Altenburg, Luuk A.; Klein, Sikke A.; Tummers, Mark J.

DOI

10.1016/j.combustflame.2025.114314

Publication date

Document Version Final published version

Published in Combustion and Flame

Citation (APA)

Altenburg, L. A., Klein, S. A., & Tummers, M. J. (2025). Flame-induced pressure gradients in turbulent premixed natural gas-air and hydrogen-air jet flames. *Combustion and Flame*, *279*, Article 114314. https://doi.org/10.1016/j.combustflame.2025.114314

Important note

To cite this publication, please use the final published version (if applicable). Please check the document version above.

Copyright

Other than for strictly personal use, it is not permitted to download, forward or distribute the text or part of it, without the consent of the author(s) and/or copyright holder(s), unless the work is under an open content license such as Creative Commons.

Please contact us and provide details if you believe this document breaches copyrights. We will remove access to the work immediately and investigate your claim.

Contents lists available at ScienceDirect

Combustion and Flame

journal homepage: www.sciencedirect.com/journal/combustion-and-flame



Flame-induced pressure gradients in turbulent premixed natural gas-air and hydrogen-air jet flames

Luuk A. Altenburg *, Sikke A. Klein, Mark J. Tummers

Department of Process & Energy (P&E), Delft University of Technology, Leeghwaterstraat 39, 2628 CB Delft, The Netherlands

ARTICLE INFO

Keywords: Hydrogen combustion Turbulent premixed jet flames Flame flashback Flame-induced adverse pressure gradient Particle image velocimetry Mie-scattering

ABSTRACT

This study focuses on flame-induced pressure gradients in turbulent premixed jet flames and its potential role in the occurrence of flame flashback. A new procedure is proposed to determine these pressure gradients experimentally from the Favre-averaged momentum equations. The procedure involves a novel experimental method to determine Favre-averaged quantities from particle image velocimetry data. The resulting pressure distributions are compared for two fuel-air mixtures with identical unstretched laminar flame speed (a stoichiometric natural gas-air mixture and a lean ($\phi = 0.49$) hydrogen-air mixture) for stable and near-flashback conditions. In all four cases the flame-induced pressure gradients are closely related to the intermittent behavior of the flame. Furthermore, the pressure gradients for the stable and near-flashback flames show only small differences indicating that the mean pressure distribution is not a suitable indicator for the occurrence of flame flashback. Detailed analysis shows a mild, but systematic shift in the orientation of the instantaneous flame fronts, which tend to align more perpendicular to the flow for the flames closer to flashback. This change in orientation results in local deceleration of the flow, thus increasing the probability of flashback.

Novelty and significance

This work presents original results of experiments in premixed hydrogen-air and natural gas-air turbulent jet flames. A new methodology is introduced to calculate Favre-averaged quantities and the pressure field in a flame from a combination of PIV and Mie scattering measurements. The focus of the experiments and follow up analyses is on the flame characteristics near flashback, since flame flashback is one of the phenomena that hampers the transition from the use of natural gas to hydrogen in, for example, gas turbines.

1. Introduction

Electrical energy production with large scale gas turbines relies on the lean premixed combustion of a fuel, traditionally natural gas, in order to meet stringent requirements on the emission of nitrogenoxides. A more recent requirement is the low, or even zero, emission of greenhouse gases. Hydrogen is considered as a very promising alternative fuel since it naturally does not contribute to the emission of carbon dioxide. When switching to hydrogen as a fuel, the gas turbine combustion system will still operate in the lean premixed mode to ensure the low nitrogen-oxide emissions. The presence of a highly reactive mixture of hydrogen and air upstream of the combustor introduces the possibility of flame flashback, i.e., the rapid upstream propagation of the flame through the burner system towards the premixing section [1]. This may lead to catastrophic failure, since these components are neither cooled nor designed to handle high temperature combustion gases. Premixed hydrogen flames have in general a much higher risk of flashback due to the inherent higher unstretched laminar flame speed. The effective

flame speed in lean premixed hydrogen flames further increases in comparison to a natural gas flame due to the nonunity Lewis number effect and the preferential diffusion effect [2]. This poses a challenge in the design of gas turbine combustion systems that run on hydrogen in lean premixed mode. Therefore, a better understanding of the flashback phenomena is required in order to design safer hydrogen-fueled gas turbine combustors.

Different flashback mechanisms have been categorized [3]. Combustion-induced vortex breakdown (CIVB) is the main mechanism for swirl stabilized flames. Hydrogen has shown to increase the risk on CIVB flashback, therefore non-swirl combustors are currently being developed for high-hydrogen fuels. In these combustors running on high-hydrogen fuels, boundary layer flashback is considered to be an important risk. Boundary layer flashback was first studied systematically by Lewis & von Elbe [4,5], who introduced the concept of a "critical velocity gradient" to predict the occurrence of flashback in laminar premixed flames produced by tube burners. While earlier

E-mail address: l.a.altenburg@tudelft.nl (L.A. Altenburg).

^{*} Corresponding author.

Nomenclature

Abbreviations

CIVB Combustion-Induced Vortex Breakdown

DNG Dutch Natural Gas
FOV Field Of View
MFC Mass Flow Controller
pdf probabilty density function
PIV Particle Image Velocimetry

Greek symbols

 α cone angle

 γ flame intermittency ϕ equivalence ratio ρ_b burnt mixture density ρ_u unburnt mixture density

 σ expansion ratio

Latin symbols

D tube inner diameter

 $\begin{array}{ll} D_{\mathrm{O}_2} & \text{mass diffusivity of the excess reactant} \\ D_f & \text{mass diffusivity of the deficient reactant} \\ D_{i/\mathrm{N}_2} & \text{mass diffusivity of fuel species } i \end{array}$

 D_T mixture thermal diffusivity

 f_i fuel volumetric fraction of fuel species i

I intensity

k turbulent kinetic energy
Le mixture Lewis number

 Le_i single fuel Lewis number of fuel species i

p pressure

 p_0 pressure at the start of the streamline

r radial coordinate

 Re_D Reynolds number based on tube inner diameter

s(r,x) streamline path

 S_{L0} unstretched laminar flame speed u_r radial velocity component u_x axial velocity component

 U_b bulk velocity

 u_b burnt mixture velocity u_u unburnt mixture velocity

x axial coordinate

H₂% volume percentage of hydrogen in the fuel

research primarily focused on flashback limits in jet flames [6,7], later studies also considered additional factors such as fuel composition, flame confinement, wall temperature and pressure [8–10].

Recent experimental studies using high-speed optical diagnostics gave new insights into flashback dynamics in bounded (confined) turbulent flows [11–14]. These studies highlight a strong coupling between the propagating flame front and the incoming flow. Regions of flow reversal were observed upstream of the flame bulges (convex-shaped towards the reactants), which intermittently form within low-velocity regions of the turbulent boundary layer, facilitating flashback. Direct numerical simulations [15] confirm the presence of flow reversal regions upstream of flame bulges and suggest that the physical mechanism behind the formation of these regions is likely to originate from the Darrieus-Landau instability, where the wrinkled flame front alters the streamline pattern and affects the pressure upstream of the flame bulge. This instability induces an adverse pressure gradient upstream

of the flame bulge, decelerating the flow and potentially causing flow reversal. In unbounded (unconfined) flame configurations, the same mechanism causes a flow retardation instead of reversal [16]. More recent DNS studies examined lean hydrogen-air premixed flame flashback in a turbulent boundary layer over a flat plate and conducted a budget analysis of the pressure transport equation, which is derived by substituting the state equation into the conservation equation for energy, to explain the presence of regions with flow reversal [17]. It was found that positive dilatation and thermal diffusivity terms near the leading edge of flame bulges are the main reason for the adverse pressure gradient. In turn, this adverse pressure gradient influences the turbulent boundary layer by enhancing the transport of low-speed fluid away from the wall and weakening high-speed flow towards the wall due to combustion, further facilitating flashback. Additional DNS studies have expanded on these findings, highlighting the impact of wall conditions on flame behavior and turbulence structure in boundary layer flashback [18].

In recent years, there has been a significant research effort focusing on flashback in premixed hydrogen combustion. All research indicates that lean premixed hydrogen-air flames show a higher propensity to flashback than can be expected from its unstretched laminar flame speed. This increased risk on flashback is attributed to the thermodiffusive instability, which is the combined effect of the nonunity Lewis number effect and the preferential diffusion effect, that occurs in lean-premixed hydrogen flames due to the high mass diffusivity of hydrogen. These effects result in a local enrichment of the flame and therefore an increase in local flame speed [19]. Similar effects of an increased turbulent flame speed can be observed in turbulent flame speed experiments for lean premixed hydrogen jet flames [20].

Recent literature on flashback in (hydrogen) flames highlights an important role of the flame-induced adverse pressure gradient. The objective of this study is to determine the flame-induced adverse pressure gradient experimentally and study its role in the local flow retardation and occurrence of flame flashback. To achieve this, a new procedure has been developed to quantify the (time-averaged) flame-induced adverse pressure using a novel method that combines Particle Image Velocimetry (PIV) and Mie-scattering measurements.

2. Methodology

This section describes the different steps in the procedure to determine the flame-induced adverse pressure gradient. The pressure gradient field will be determined by experimentally solving all other terms in the Favre-averaged equations of motion, as described in Section 2.1. Experimentally solving the different terms in these equations requires determining Favre-averaged quantities. These can be obtained from PIV data using a procedure that relies on detailed information on the instantaneous flame front location in each instantaneous PIV image, as explained in Section 2.2. Finally, Section 2.3 presents the flame front detection method that was used in the present study.

2.1. Favre-averaged equations of motion

The Favre-averaged equations for continuity and radial and axial momentum in cylindrical coordinates are used to determine the pressure gradient field. This is based on the assumption of an axisymmetric mean flow and neglecting viscous effects. The continuity equation in dimensionless form is given by:

$$\nabla^* \cdot \overline{\rho^* \mathbf{u}^*} = \frac{\partial}{\partial x^*} (\overline{\rho^* u_x^*}) + \frac{1}{r^*} \frac{\partial}{\partial r^*} (r^* \overline{\rho^* u_r^*}) = 0,$$

$$(1)$$
Mass flux

where \mathbf{u} denotes the velocity vector with components u_r and u_x . An overline denotes Reynolds averaging and a tilde denotes Favre averaging. Furthermore, a superscript * is used to denote dimensionless

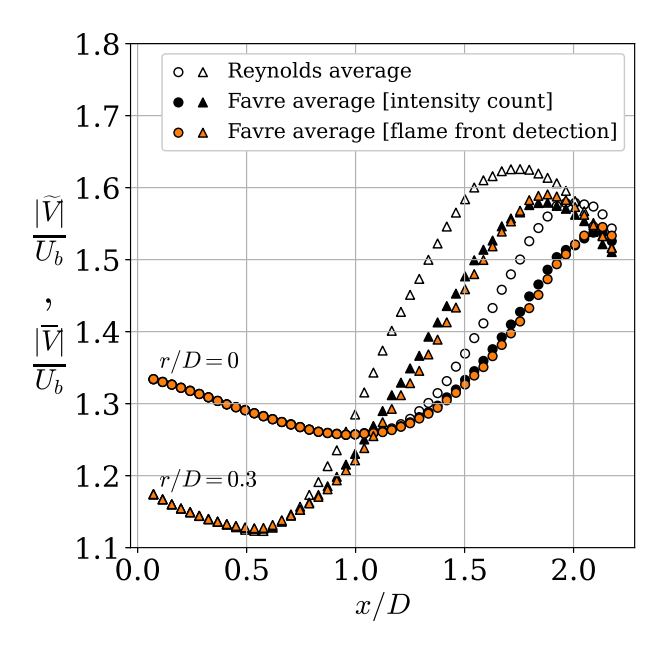


Fig. 1. The dimensionless Favre-averaged velocity magnitude $|\widetilde{V}|/U_b$ and the dimensionless Reynolds-averaged velocity magnitude $|\widetilde{V}|/U_b$ along vertical lines at r/D=0 (spheres) and r/D=0.3 (triangles), starting just above the burner exit at $x/D\approx0.1$. The black and orange markers indicate the two Favre-averaging procedures: the black markers represent the procedure that directly couples gas density to the intensity count, while the orange markers represent the procedure combining flame front detection with bimodal behavior.

quantities defined as:

$$\nabla^* = D\nabla, \quad u^* = \frac{u}{U_b}, \quad \rho^* = \frac{\rho}{\rho_u},$$

$$r^* = \frac{r}{D}, \quad x^* = \frac{x}{D}.$$
(2)

The dimensionless equations for axial and radial momentum are given by Eqs. (3) and (4), respectively:

$$\overline{\rho^* u_x^*} \frac{\partial \widetilde{u}_x^*}{\partial x^*} + \overline{\rho^* u_r^*} \frac{\partial \widetilde{u}_x^*}{\partial r^*} =$$

$$-\frac{\partial \overline{\rho^*}}{\partial x^*} - \underline{\frac{\partial F_{xx}^*}{\partial x^*}} - \underline{\frac{1}{r^*}} \frac{\partial (r^* F_{rx}^*)}{\partial r^*}$$
Change in

Change in

Change in

$$\overline{\rho^* \widetilde{u}_x^*} \frac{\partial \widetilde{u}_r^*}{\partial x^*} + \overline{\rho^* \widetilde{u}_r^*} \frac{\partial \widetilde{u}_r^*}{\partial r^*} =$$

$$\xrightarrow{\text{Axial advection advection}}$$

$$-\frac{\partial \overline{\rho^*}}{\partial r^*} - \underbrace{\frac{\partial F_{rx}^*}{\partial x^*}}_{\text{Change in gradient Favre shear stress}} - \underbrace{\frac{1}{r^*} \frac{\partial (r^* F_{rr}^*)}{\partial r^*}}_{\text{Change in Favre normal stress}}, (4)$$

where p^* denotes the dimensionless pressure as in $p^* = p/(\rho_u U_b^2)$ and the dimensionless Favre stress terms F_{rr}^* , F_{rx}^* and F_{xx}^* are given by:

$$F_{rr}^* = \overline{\rho^*} \widetilde{u_r''^* u_r''^*}, F_{rx}^* = \overline{\rho^*} \widetilde{u_r''^* u_x''^*}, F_{xx}^* = \overline{\rho^*} \widetilde{u_x''^* u_x''^*}.$$

Prior to determining the pressure gradient terms in Eqs. (3) and (4), the Reynolds-averaged dimensionless density field $\overline{\rho^*}$, as well as the Favre-averages $\widetilde{\varphi^*} = \overline{\rho^* \varphi^*}/\overline{\rho^*}$ of a dimensionless quantity φ^* have to be determined. The next section evaluates two procedures that can be used to extract these quantities from a PIV measurement.

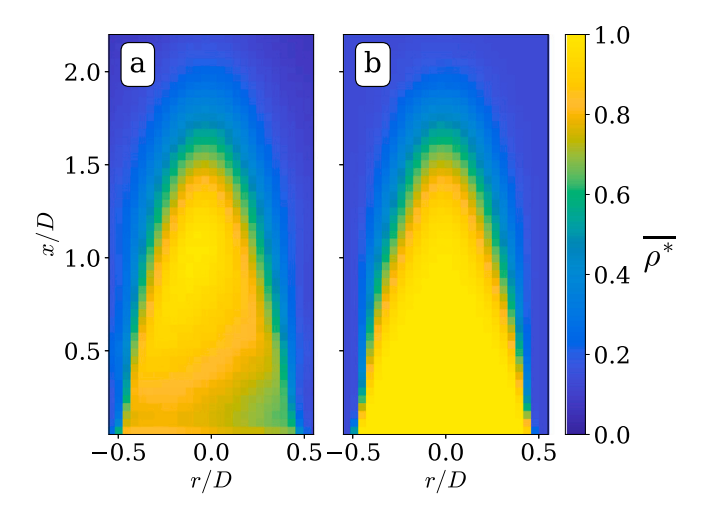


Fig. 2. (a) The Reynolds-averaged density field $\overline{\rho^*}$ for both procedures: (a) The first procedure, where $\overline{\rho^*} \equiv \overline{I}/\overline{I}_{max}$, shows a density field that is clearly not symmetric in r. (b) The second procedure, where the Reynolds-averaged density field $\overline{\rho^*}$ follows from the flame front detection method combined with the bimodal behavior, shows a symmetric density field.

2.2. Reynolds- and Favre-averaged quantities from PIV data

In standard PIV the mean of a velocity component u in a particular interrogation area is determined from the arithmetic mean of all instantaneous velocities $u(t_i) = u_i$ for that interrogation area as in:

$$\overline{u} = \frac{1}{N} \sum_{i=1}^{N} u_i,\tag{5}$$

where N is the total number of instantaneous images in a PIV measurement. This results in a Reynolds-averaged velocity component. However, in combustion studies one is often interested in Favre-averaged (density-weighted) quantities. In that case each instantaneous velocity u_i has to be weighted with the instantaneous gas density $\rho(t_i) = \rho_i$ as in:

$$\widetilde{u} = \sum_{i=1}^{N} \rho_i u_i / \sum_{i=1}^{N} \rho_i. \tag{6}$$

Clearly, determining a Favre-averaged velocity component in a particular interrogation area requires information on both the instantaneous velocity and the instantaneous gas density in that interrogation area. The latter is not directly available from PIV, but there are procedures to estimate the instantaneous density from the PIV measurements, and two of these procedures will be discussed below.

In the first procedure it is assumed that the instantaneous number of seeding particles $n(t_i) = n_i$ in an interrogation area is (on average) proportional to the gas density ρ_i when the seeding particles do not burn or evaporate in the flame. In a further simplification it is assumed that n_i is proportional to the sum of the pixel intensities in an interrogation area $I(t_i) = I_i$. Thus, a Favre-averaged velocity component can be determined from Eq. (6) by replacing ρ_i with I_i .

The second procedure involves examining each instantaneous PIV velocity vector and its corresponding PIV interrogation window. If an interrogation window is entirely within the unburnt region, the instantaneous density ρ_i is assumed to be equal to the unburnt mixture density ρ_u . Conversely, for an interrogation window fully within the burnt region, the instantaneous density ρ_i is set to that of the burnt mixture ρ_b . For interrogation windows that cover both burnt and unburnt areas, the instantaneous density ρ_i is calculated using an area-weighted average of ρ_u and ρ_b . Pfadler et al. [21] employed a comparable procedure named as conditioned particle image velocimetry. The values of the unburnt and burnt mixture densities are determined using Cantera

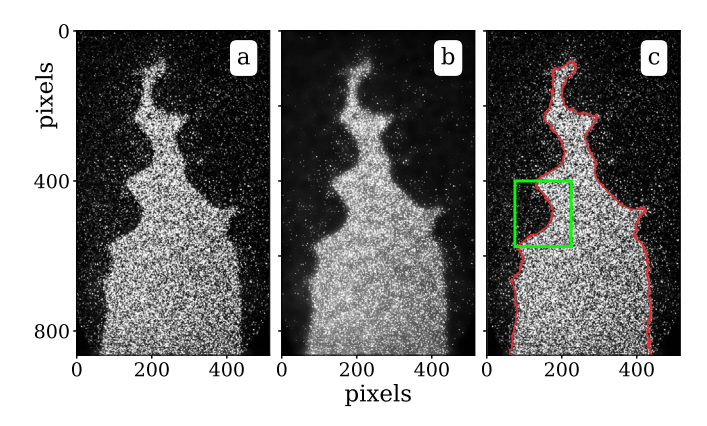


Fig. 3. Main steps of the flame front detection method applied to one of the premixed jet flames considered in this study: (a) Raw Mie-scattering image (b) Image after normalization and applying the bilateral filter (c) Mie-scattering image with the detected flame front. The green box indicates the region that is magnified in Fig. 5.

2.6. Clearly, the second procedure relies on an accurate determination of the flame front in each instantaneous PIV image. The flame front detection method used in the present work is described in Section 2.3.

As an illustration, Fig. 1 shows Reynolds-averaged and Favreaveraged velocities (for both procedures) as determined in one of the premixed jet flames considered in this work, see Section 3.2 for details. To be more precise, the graph displays the profiles of the dimensionless Favre-averaged velocity magnitude $|\tilde{V}|/U_b$ for both procedures, along with the dimensionless Reynolds-averaged velocity magnitude $|\overline{V}|/U_h$ along vertical lines at r/D=0 (spheres) and r/D = 0.3 (triangles), starting just above the burner exit at $x/D \approx 0.1$. It can be seen from this figure that the two procedures to produce Favreaveraged velocities show very similar results. Furthermore, it can be observed that both the Favre-averaged velocity profiles start to deviate from the Reynolds-averaged velocity profile around $x/D \approx 1.25$ (for r/D=0) and $x/D\approx 0.75$ (for r/D=0.3). This is due to the intermittent presence of the flame. Fig. 2a shows the estimation of the Reynoldsaveraged density field $\overline{\rho^*}$ from the first procedure, where $\overline{\rho^*} \equiv \overline{I}/\overline{I}_{max}$ with \overline{I}_{max} the maximum of the Reynolds-averaged intensity field. An inhomogeneous dimensionless Reynolds-averaged intensity field within the cone is observed, where a Reynolds-averaged density field that is symmetric in the radial coordinate r is expected. This inhomogeneity is associated with the inhomogeneous intensity of the laser light sheet, which results in an inhomogeneous illumination of the seeding particles and, consequently, an inaccurate density field. Fig. 2b shows the Reynolds-averaged density field as determined from the second procedure, which in case of determining the density is directly linked to the flame intermittency function, γ , which is defined here as the fraction of time that products are found at a location so that $\gamma = 1$ corresponds to pure products and $\gamma = 0$ corresponds to pure reactants. The Reynolds-averaged density $\overline{\rho^*}$ then follows from $\overline{\rho^*} = \rho_u(1-\gamma) + \rho_b \gamma$. It is seen in Fig. 2b that the inhomogeneity of the laser light sheet did not produce an asymmetry in the density field. This is due to the fact that the flame front detection method, which is an essential part of the second method, is insensitive to inhomogeneities in the laser light sheet. Since the Reynolds-averaged density $\overline{\rho^*}$ occurs in the equations of motion (Eqs. (3) and (4)) it was decided to use the second procedure in the remainder of this work.

2.3. Flame front detection method

The method that is used to determine the instantaneous flame front in this study is based on the work of Pfadler et al. [21], where the location of the flame front in an instantaneous PIV image was identified from the variation of the local particle number density using

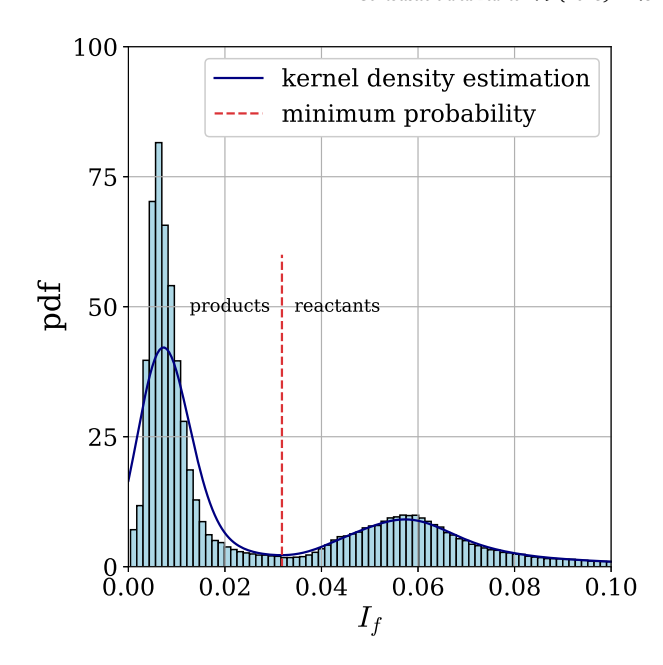


Fig. 4. The distribution of the filtered intensity I_f after applying the bilateral filter with a fitted distribution using a kernel density estimation. The dashed line indicates the filtered intensity at minimum probability of the fitted distribution, which separates the products from the reactants.

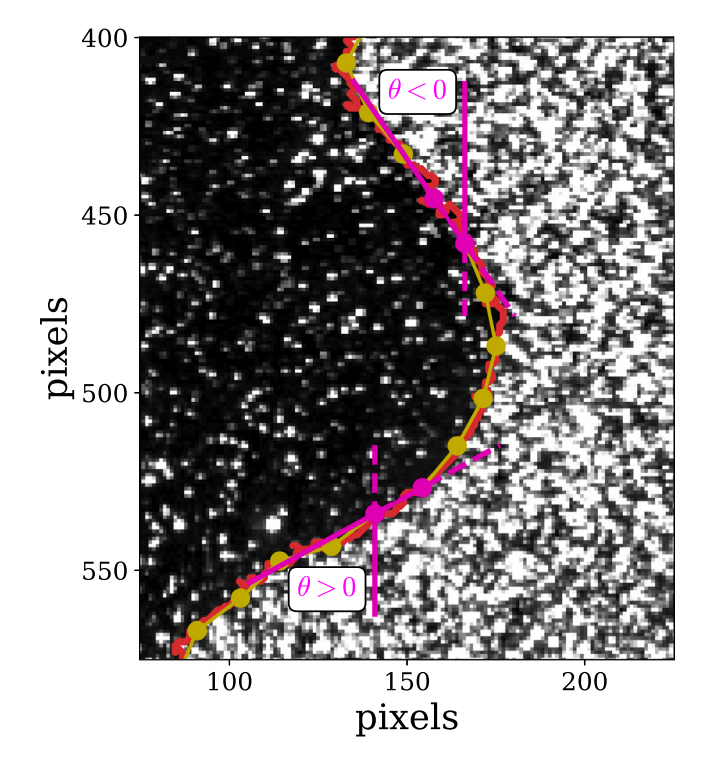


Fig. 5. Segmentation of the detected flame front after binarizing the image (red line) into equidistant segments (yellow line). Two segments (magenta) are used to illustrate the definition of the local flame front segment angle θ , which is defined as the acute angle between the local flame front segment and the vertical. The region displayed in this figure corresponds to the green box in Fig. 3c.

only spatial data of a raw Mie-scattering image. Zheng et al. [22] further refined the flame front detection method by introducing some intermediate steps for determining the local particle number density. The present study proposes a new approach to identify the variation of the local particle number density and thus the location of the flame

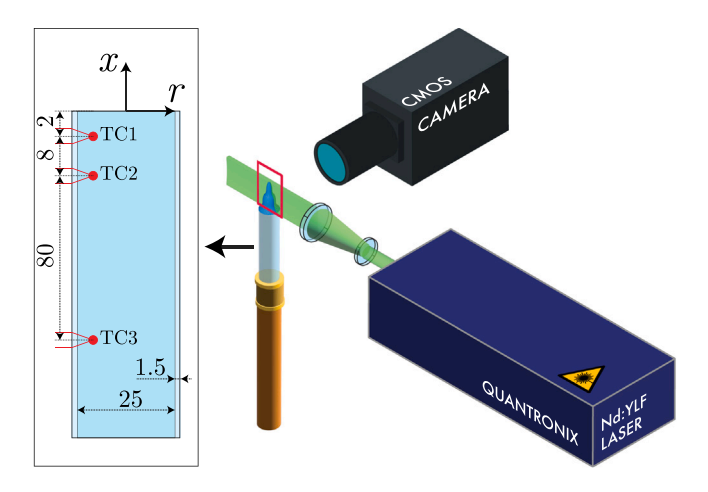


Fig. 6. Left: The quartz tube and thermocouple locations. The dimension are in mm. Right: A schematic of the diagnostic setup. The field of view (FOV) of the PIV system is indicated by the red rectangle.

front. This new approach combines both spatial and intensity data in the Mie-scattering image without the need for intermediate steps. The method involves the application of the bilateral filter as described by Tomasi & Manduchi [23] to extract the filtered intensity I_f of a PIV image, which is then further processed using a histogram function. A bilateral filter is a nonlinear filter that smooths the image while preserving edges, which makes it suitable for flame front detection. The filter applies a weighting function to each pixel in the image based on its intensity difference with neighboring pixels, as well as its spatial distance from those pixels. The weighting function uses two Gaussian kernels, i.e. a spatial kernel and an intensity kernel. The two kernels are characterized by the spatial standard deviation σ_s , the intensity standard deviation σ_I and a spatial parameter d_{size} , which is the diameter of each pixel neighborhood that is used during filtering. The spatial standard deviation parameter σ_s was set to $d_{size}/2$, which results in a spatial kernel that has a full-width-at-half-maximum equal to d_{size} . The intensity standard deviation parameter σ_I was assigned a value of 0.1, which corresponds to 10% of the maximum intensity range of the image. The parameter controlling the size of the bilateral filter d_{size} was set such that it corresponds to the number of pixels covering a physical distance of 2 mm.

Figs. 3 and 4 illustrate the new method. First, the intensity of the raw Mie-scattering image, shown in Fig. 3a, is normalized. Second, the bilateral filter is applied to the normalized Mie-scattering image, resulting in the filtered image shown in Fig. 3b. Then the histogram of the filtered image intensity was calculated (Fig. 4) and a kernel density estimation was applied to fit a continuous function to the histogram, resulting in two easily discernible peaks corresponding to the unburnt (reactants) and burnt (products) regions. To accurately distinguish these regions, the threshold for the filtered pixel intensity was set to the intensity value at minimum probability in between both peaks. The flame front was then determined by setting the threshold to this level and binarizing the image. The resulting flame front is shown as a red line in Fig. 3c. As a final step, the detected flame front was divided into equidistant segments of 1 mm. This segmentation smooths the detected flame front and eliminates artificial wrinkling, as illustrated in Fig. 5. The figure also shows the definition of the local flame front segment angle θ , which is a crucial parameter for interpreting the results in this work. It is defined as the acute angle between the local flame front segment and the vertical. A positive value of θ indicates that locally the burnt region is positioned above the unburnt region, whereas a negative value indicates the opposite. Higher positive (negative) values indicate a more horizontal segment.

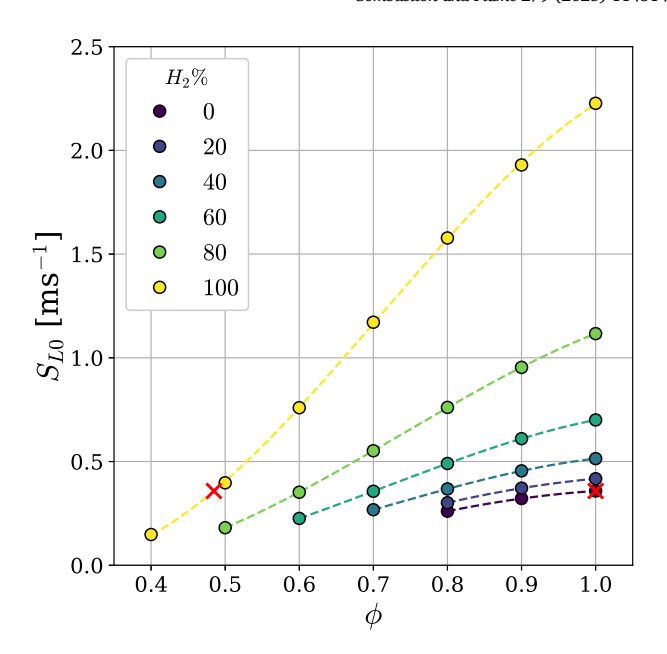


Fig. 7. Unstretched laminar flame speed S_{L0} as a function of equivalence ratio ϕ for several ${\rm H_2/DNG}$ -air mixtures. The values of S_{L0} were calculated by using a one-dimensional simulation in Cantera 2.6. The red crosses mark the two mixtures that were analyzed extensively in this work.

3. Experimental setup

3.1. Burner and flame conditions

Experiments were conducted on turbulent premixed jet flames produced by a quartz tube Bunsen burner with an internal diameter of $D=25\,\mathrm{mm}$ and a wall thickness of 1.5 mm, see Fig. 6 (left). The tube was equipped with three K-type thermocouples installed on the outer wall at 2 mm, 10 mm and 90 mm from the burner exit to monitor the burner temperature. In this study an r, x-coordinate system will be used with its origin at the center of the tube exit. The x-coordinate is measured vertically upward.

The fuel and air are premixed at a distance sufficiently far upstream from the burner exit to ensure a uniform fuel-air mixture at the burner exit. The fuels considered in this study are mixtures of hydrogen and Dutch Natural Gas (DNG) [24]. The approximate composition of DNG is 81% methane, 4% ethane, 14% nitrogen and 1% higher alkanes by volume. The fuel and air flows are determined by using three Bronkhorst® mass flow controllers (MFCs) for air, H2 and DNG. LabView was used to set and monitor the MFCs. Three experimental parameters were varied in this study, i.e. the Reynolds number Re_D (through the bulk velocity U_b), the equivalence ratio ϕ and the volume percentage of hydrogen in the fuel H₂%. The Reynolds number is based on the internal diameter of the pipe and the bulk velocity, which is computed using the flow rates from the MFC readings (corrected for deviations from the normal pressure and normal temperature). The kinematic viscosity was calculated using Cantera 2.6, which uses Wilke's rule [25]. A UV sensor was installed close to the burner exit to detect the presence of the flame and to cut the supply of fuel in case of a flashback or blow-off.

3.2. Experimental program

In this work two experiments were conducted on premixed turbulent $\rm H_2/DNG$ -air jet flames under atmospheric conditions. Experiment I involved an exploration of the flashback limits for six $\rm H_2/DNG$ -air mixtures at varying equivalence ratios. For a given fuel-air mixture, characterized by ϕ and $\rm H_2\%$, the flame was ignited at a Reynolds number that resulted in a stable flame. The flashback experiment was

Table 1
Specifications of the premixed jet flames considered in experiment II.

Case	Re_D	$egin{aligned} U_b \ igl[\mathrm{m}\mathrm{s}^{-1} igr] \end{aligned}$	φ	$H_2\%$	Le	D_f/D_{O_2}	Condition	$Re_{D,fb}$	$egin{aligned} U_{b,fb} \ igl[\mathrm{m}\mathrm{s}^{-1} igr] \end{aligned}$
DNG-4000	4000	2.5	1.00	0	1.02	1.06	stable	2700	1.7
DNG-3000	3000	1.9	1.00	0	1.02	1.06	near-flashback	2700	1.7
H ₂ -16000	16000	11.6	0.49	100	0.43	3.74	stable	11 900	8.6
H ₂ -12500	12500	9.1	0.49	100	0.43	3.74	near-flashback	11 900	8.6

started after a constant burner tip temperature was reached. Flashback was subsequently induced by decreasing the Reynolds number (bulk velocity) incrementally, while keeping the mixture properties constant. Each experiment was repeated three times to obtain an impression of the variation between runs.

Experiment II considers two mixtures that were examined more extensively in this work, i.e. a stoichiometric DNG-air mixture and a lean H2-air mixture. For each mixture, two Reynolds numbers were considered corresponding to (1) a stable flame and (2) a flame nearflashback, see Table 1 for details. The table also features the flashback limits in terms of the Reynolds number (bulk velocity) at flashback $Re_{D,fh}(U_{h,fh})$ for the two mixtures. It is important to realize that both types of flames ("stable" and "near-flashback") are stable flames, but the latter is closer to flashback than the former. The stable flames operate at 48% and 34% above the flashback limit for the DNG-air mixture and the H₂-air mixture, respectively. The near-flashback flames operate at 11% and 5% above the flashback limit for the DNG-air mixture and the H₂-air mixture, respectively. The mixtures were chosen such that their computed unstretched laminar flame speed S_{I0} was approximately $0.36\,\mathrm{m\,s^{-1}}$, see Fig. 7. The unstretched laminar flame speed was calculated using a one-dimensional simulation in Cantera 2.6 for a freely-propagating premixed laminar flame using the detailed reaction mechanism GRI-Mech 3.0 [26]. The mixture Lewis number Le was calculated using the volumetric weighted approach as described by Muppala et al. [27]:

$$Le = \sum_{i} f_i Le_i, \tag{7}$$

where Le_i represents the single fuel Lewis number for species i and f_i denotes the fuel volumetric fraction of species i. The single fuel Lewis number Le_i is expressed as:

$$Le_i = \frac{D_T}{D_{i/N_2}},\tag{8}$$

where D_T is the mixture thermal diffusivity and $D_{i/{\rm N}_2}$, the mass diffusivity of the deficient fuel species i, conventionally taken as the reactant-inert binary diffusion coefficient. The preferential diffusion effect is characterized by the mass diffusivity ratio $D_f/D_{\rm O_2}$, with the mass diffusivity of the deficient reactant D_f and the mass diffusivity of the excess reactant $D_{\rm O_2}$. $D_{\rm O_2}$ is taken as the oxygen-inert binary diffusion coefficient $D_{\rm O_2/N_2}$. Similarly to the calculation of the mixture Lewis number, the value of D_f is calculated using a volumetric weighted approach as:

$$D_f = \sum_i f_i D_{i/N_2}. (9)$$

The values of D_T , D_{i/N_2} and $D_{{\rm O}_2/N_2}$ were all obtained from Cantera 2.6 using properties of the unburnt mixture.

3.3. Diagnostic setup

Particle Image Velocimetry (PIV) was used to obtain quantitative and qualitative data on the velocity fields. The flow was seeded with aluminum-oxide particles (Al $_2$ O $_3$) with a mean diameter of 1 μ m. A Nd:YLF dual-cavity laser (Quantronix Darwin-Duo Pro527-80-M) emitting a beam of green light (at 527 nm wavelength) was used to illuminate the particles. The laser beam was transformed into a laser

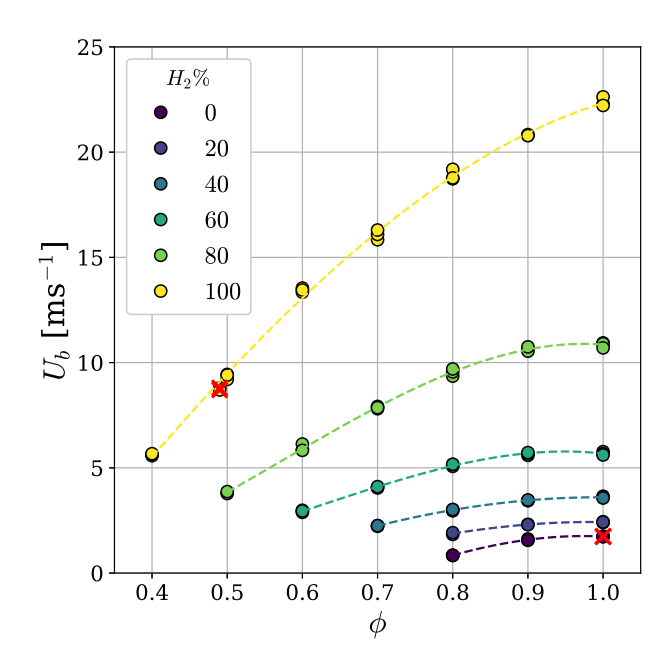


Fig. 8. Bulk velocity U_b at flashback as a function of the equivalence ratio ϕ for several H₂/DNG-air mixtures. The red crosses mark the two mixtures studied in detail in this work.

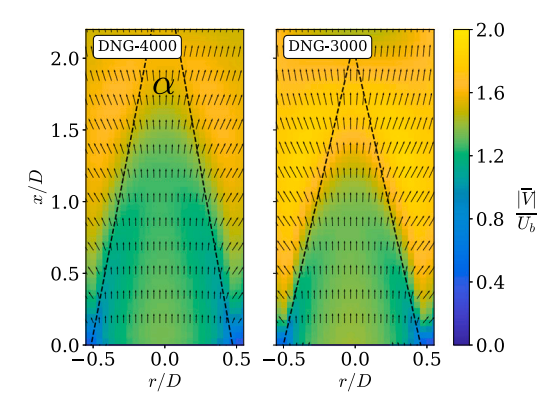
sheet with a thickness of approximately 1 mm using a system of planoconcave and convex lenses. A schematic of the setup is shown in Fig. 6 (right).

The illuminated particles were imaged on the CMOS sensor of a Photron Fastcam SA1.1 high-speed camera fitted with a Nikkor 200 mm lens (f $^{\#}$ = 8). The CMOS sensor, which has a resolution of 1024×1024 pixels each with a size of $20\,\mu\text{m} \times 20\,\mu\text{m}$, was cropped to 896×512 pixels resulting in a field of view of approximately $59\,\text{mm} \times 33\,\text{mm}$.

The premixed jet flames in experiment II were imaged using both low- and high-speed PIV recordings. The low-speed recordings were taken to obtain time-averaged statistics of the reacting flow field, whereas the high-speed recordings were taken to capture flame-flow interaction and flashback in a time-resolved fashion. For the low-speed recordings the frame rate was set to $0.05\,\mathrm{kHz}$ and a total of 2500 image pairs were collected, whereas for the high-speed recordings the frame rate was set to $2\,\mathrm{kHz}$ and $6.25\,\mathrm{kHz}$ with a total of 5000 image pairs taken for the DNG-air flame and the $\mathrm{H_2}$ -air flame, respectively.

A LaVision programmable timing unit was used to synchronize the laser pulses and the high-speed camera. The time interval, Δt , separating two consecutive pulses of the laser, has been set to obtain an average particle displacement of around 8–15 pixels. Both the acquisition and processing of the PIV images were carried out using Davis 10.2 (LaVision). A multi-pass cross-correlation approach, one pass with an interrogation window of 64×64 pixels and three passes with an interrogation window of 16×16 pixels was used. The interrogation windows had no overlap. Post-processing of the velocity vectors was done by means of a median filter with universal outlier detection to remove spurious vectors.

In addition to the velocity field extraction, the raw Mie-scattering images were also utilized to detect the instantaneous location and



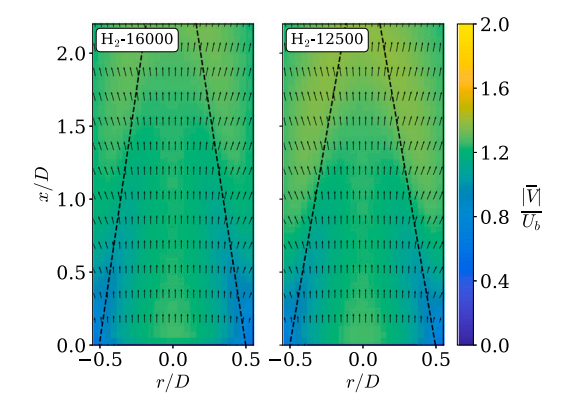


Fig. 9. The Reynolds-averaged velocity vectors for the DNG-air flames (DNG-4000, DNG-3000) and the H_2 -air flames (H_2 -16000, H_2 -12500). The background color corresponds to the dimensionless velocity magnitude $|\overline{V}|/U_b$ and the dashed lines represent the flame cones constructed using the method described in the Appendix. The angle between the dashed lines corresponds to the cone angle α .

shape of the flame front. The flow seeded with particles experiences an acceleration across the flame front due to a sudden change in gas density, resulting in a corresponding change in seeding particle density. Although the sharp interface between these two regions solely distinguishes the high-density unburnt gas and the low-density burnt gas, in this study it was interpreted as the instantaneous flame front. The method described in Section 2.3 was applied to extract the instantaneous flame front from the Mie-scattering images of the DNG-air and $\rm H_2$ -air flames.

4. Results

4.1. Flashback propensity map

Flashback propensity is defined here as the bulk velocity U_b at flashback as a function of the equivalence ratio ϕ . Fig. 8 shows the flashback propensity map that was determined in Experiment I. As expected, the flashback propensity increases with the equivalence ratio for all fuel-air mixtures considered in this study. It is also seen that there is a non-linear increase of the bulk velocity at flashback with the hydrogen content in the fuel, i.e. the flashback propensity is strongly increasing with the volume percentage of hydrogen in the fuel, H₂%.

A comparison of the data points marked by the red crosses in Figs. 7 and 8 indicate that the bulk velocity at flashback significantly exceeds the unstretched laminar flame speed. More specific, the ratio of the bulk velocity at flashback to the unstretched laminar flame speed $U_{b,fb}/S_{L0}\approx 24$ for 100% H_2 at an equivalence ratio $\phi=0.49$ and $U_{b,fb}/S_{L0} \approx 5$ for 100% DNG at $\phi = 1.00$. This difference is speculated to result from nonequidiffusion effects, which affect the considered H₂-air and DNG-air turbulent jet flames in different ways. The effects of both the low Lewis number of the premixed H2-air flame (Le=0.43) and the high diffusivity of hydrogen ($D_f/D_{\mathrm{O}_2}=3.74$) lead to stronger transport of hydrogen towards the regions of the flame front that are convex-shaped towards the reactants. This increased diffusion of hydrogen causes local enrichment, resulting in a higher equivalence ratio and, consequently, higher flame speeds [2,19]. In the considered natural gas-air flames, where diffusivities are nearly equal (Le = 1.02 and D_f/D_{O_2} = 1.06), these effects have only a minor influence on the flame speed.

4.2. The effect of the flame front on the flow field

4.2.1. Flow acceleration through the flame front

Fig. 9 shows the Reynolds-averaged velocity vectors for the two mixtures at both low and high Reynolds numbers in Experiment II. The background color represents the dimensionless velocity magnitude $|\overline{V}|/U_b$. The black dashed lines indicate the flame cone as constructed

Table 2
Velocity ratio calculations using Eq. (10) for the premixed jet flames considered in experiment II.

Case	ρ_u/ρ_b	α [°]	u_b/u_u
DNG-4000	7.6	21	1.4
DNG-3000	7.6	26	1.7
H ₂ -16000	5.0	17	1.1
H ₂ -12500	5.0	20	1.3

using the method described in the Appendix. The flame cone is the approximate time-averaged location of the flame front. It is seen that for a given mixture the velocity increase across the flame front increases as the Reynolds number decreases, consistent with the fact that the cone angle α increases with decreasing Reynolds number, see Table 2 for details.

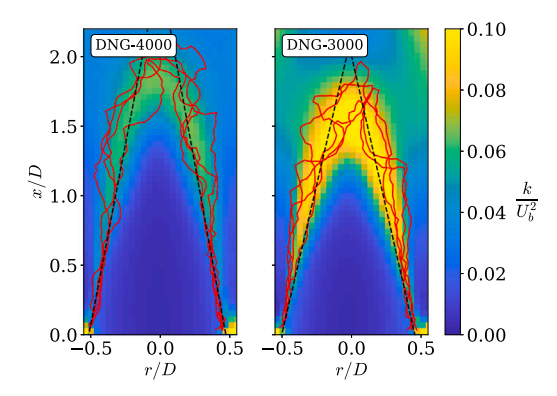
By comparing the results of the DNG-air and H_2 -air mixtures in Fig. 9 it can be seen that the flow acceleration through the flame front is larger for the DNG-air flame as compared to the H_2 -air flame. It follows from mass conservation that the higher velocity ratio u_b/u_u can be attributed to the larger cone angle α and the higher expansion ratio ρ_u/ρ_b of the DNG-air flames compared to the H_2 -air flames. The larger cone angle results in a smaller burnt surface area A_b . A simple derivation shows that the ratio A_u/A_b is proportional to $\sin{(\alpha/2)}$ as in:

$$\frac{u_b}{u_u} = \frac{\rho_u}{\rho_b} \frac{A_u}{A_b} \sim \frac{\rho_u}{\rho_b} \sin\left(\frac{\alpha}{2}\right). \tag{10}$$

In the present experiment the expansion ratio ρ_u/ρ_b was estimated from one-dimensional adiabatic flame calculations in Cantera 2.6. The calculated expansion ratios are $\rho_u/\rho_b=7.6$ and $\rho_u/\rho_b=5.0$ for the DNG-air flame and H₂-air flame, respectively. Table 2 displays the calculated velocity ratios u_b/u_u obtained by substituting the flame cone angle α and the expansion ratios ρ_u/ρ_b into Eq. (10). Comparing these velocity ratios with the velocity increase observed across the time-averaged flame front in Fig. 9, it is apparent that Eq. (10) can serve as a rule of thumb for estimating the velocity increase across the flame front.

4.2.2. Flame-generated turbulence

Fig. 10 shows the dimensionless turbulent kinetic energy k/U_b^2 for the DNG-air and H_2 -air flames for stable conditions (DNG-4000 and H_2 -16000) and near-flashback conditions (DNG-3000 and H_2 -12500). The value of k was determined as $k = \frac{1}{2}(\overline{u_r'^2} + \overline{u_x'^2})$, i.e., the value of k is based on Reynolds averages, as is commonly done in PIV studies in combustion. This figure shows that the dimensionless turbulent kinetic energy in the DNG-air flames is higher than that in the H_2 -air flames. Additionally, for the DNG-air flames the turbulent kinetic energy has a maximum near the cone tip, while in the H_2 -air flames



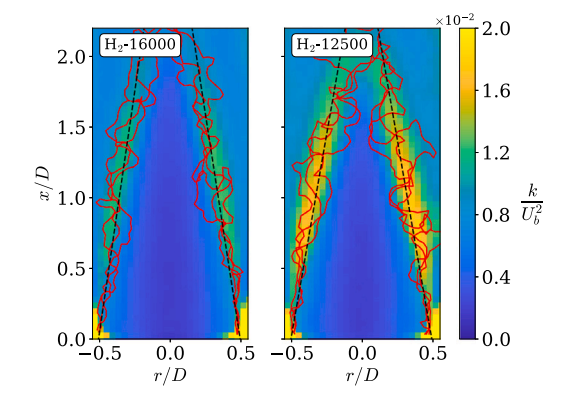
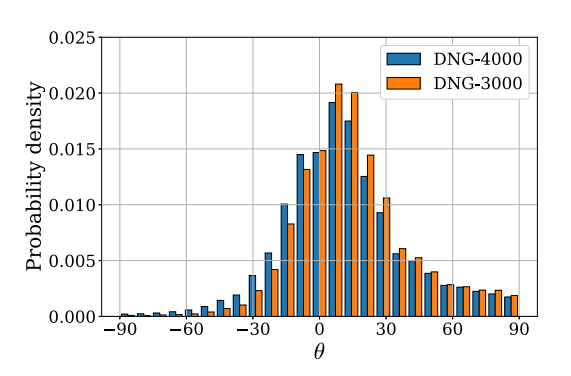


Fig. 10. Dimensionless turbulent kinetic energy field k/U_b^2 for the DNG-air flames (DNG-4000, DNG-3000) and H_2 -air flames (H_2 -16000, H_2 -12500). The dashed lines represent the flame cones constructed using the method described in the Appendix. The red lines represent instantaneous flame fronts at arbitrary instants in time.



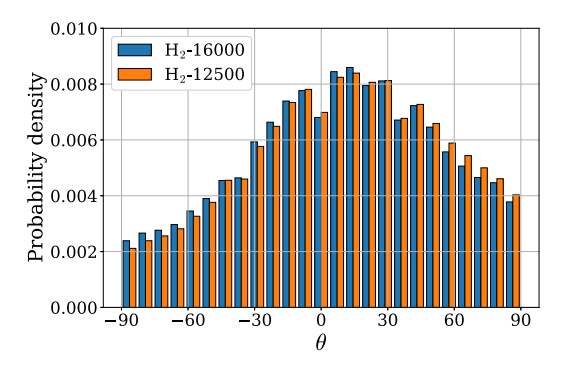
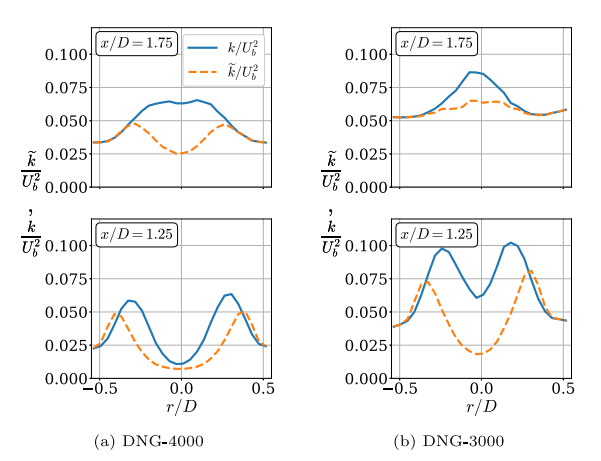
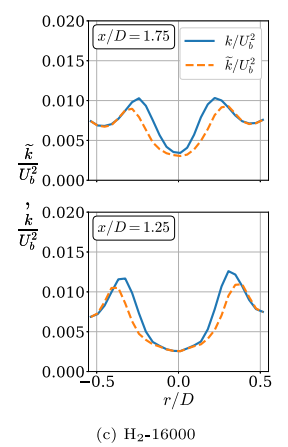


Fig. 11. Probability density of the local flame front angle θ for the DNG-air flames (left) and H₂-air flames (right).





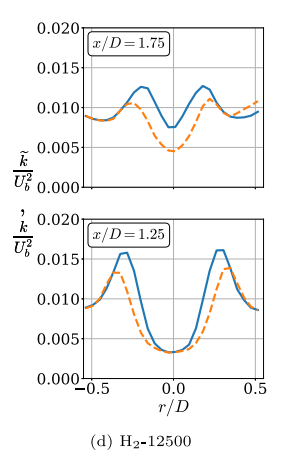


Fig. 12. Comparison of the Reynolds-averaged (k) and Favre-averaged (\tilde{k}) version of the turbulent kinetic energy along the lines x/D=1.25 and x/D=1.75 for the DNG-air flames (DNG-4000, DNG-3000) and H₂-air flames (H₂-16000, H₂-12500).

the highest values are found on the flanks of the flame cone. The elevated turbulent kinetic energy at the edge of the burner exit can be attributed to experimental artifacts. In the direct vicinity of the edge of the burner exit, the PIV algorithm regularly produces incorrect velocity vectors because the surrounding (laboratory) air is unseeded. This leads to regions where the PIV algorithm detects either artificially high or low velocities, which in turn result in high velocity fluctuations, and subsequent high values of the turbulent kinetic energy in these regions. Therefore, these elevated turbulent kinetic energy values are not related to the combustion process but rather to the limitations of the PIV measurement in these regions. A comparison of the DNG-4000 case in Fig. 10 and the probability density function of the flame front location in Fig. A.23(a) shows that the region with significant turbulent kinetic energy matches the region with high intermittency

of the flame front. Due to the intermittency, a fixed position in space is either in the unburnt region, with relatively low velocities, or in the burnt region, with relative high velocities. In the time averaging of instantaneous snapshots the relatively large velocity differences between burnt and unburnt velocities are interpreted as turbulent fluctuations thus resulting in relatively large values of turbulent kinetic energy.

The visualization of the instantaneous flame fronts in Fig. 10 illustrates that the near-flashback flames, DNG-3000 and $\rm H_2$ -12500, have fronts with larger indentations and bulges resulting in higher turbulent kinetic energy compared to their stable counterparts, DNG-4000 and $\rm H_2$ -16000. Additionally, the local orientation of the flame front contributes to these increased values. When the flame bulges develop, there are more flame front segments that have a large angle with respect to the vertical, resulting in higher values of the velocity

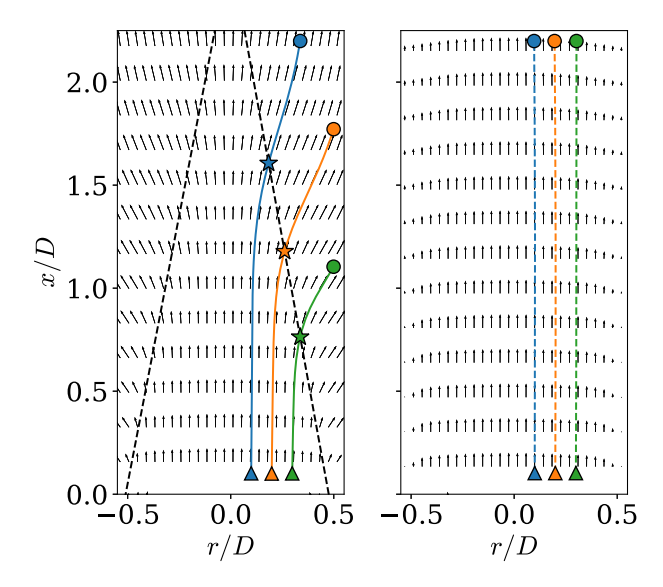


Fig. 13. The Reynolds-averaged velocity vectors with streamlines for (left) a reacting flow, i.e. DNG-4000 and (right) a non-reacting flow. The blue, orange and green streamlines are starting at radial positions r/D=0.1, r/D=0.2 and r/D=0.3, respectively, and at an axial position x/D=0.1. The black dashed lines represent the flame cone. The triangles and spheres mark the start and end point of the corresponding streamline, respectively. The stars mark the intersection of the flame cone and the corresponding streamline.

ratio u_b/u_u across the front, which further elevates the values of k/U_b^2 . Fig. 11 shows the probability density of the local flame front segment angle θ for all instantaneous images for the flame fronts located between $0.25 \le x/D \le 1.25$ for the DNG-air flames and H₂-air flames. This specific range was chosen because it is close to the burner exit, where flashback occurs, and it aligns with the axial locations used to construct the flame cone (see Fig. A.23). The definition of the local flame front segment angle θ is given in Fig. 5. In Fig. 11, a slight shift towards higher values of θ is observed when comparing the stable flames (DNG-4000, H₂-16000) to the near-flashback flames (DNG-3000, H₂-12500). Furthermore, the probability density analysis of the local flame front segment angle θ shows that the H₂-air flames exhibit more horizontally oriented segments than the DNG-air flames. This indicates that the H₂-air flames exhibit a more wrinkled flame front.

Like mentioned before the turbulent kinetic energy was computed using Reynolds-averaged quantities as $k=\frac{1}{2}(\overrightarrow{u_1'^2}+\overrightarrow{u_x'^2})$. It is interesting to consider the Favre-averaged version of the turbulent kinetic energy, i.e., $\widetilde{k}=\frac{1}{2}(\overrightarrow{u_1''^2}+\overrightarrow{u_x''^2})$ where the Favre-averaged quantities are determined using the second method described in Section 2.2. Fig. 12 compares the values of k and \widetilde{k} along the lines x/D=1.25 and x/D=1.75. The figure shows that the DNG-air flames exhibit more pronounced differences between k and \widetilde{k} than the H_2 -air flames, which is due to the larger differences in density between the burnt and unburnt regions for the stoichiometric DNG-air flame as compared to the lean H_2 -air flame. As a consequence, directly comparing the turbulent kinetic energy obtained from standard PIV experiments (typically yielding k) with the results of numerical simulations (where typically \widetilde{k} is computed) is not a valid approach and can lead to incorrect conclusions regarding the accuracy and performance of the numerical model.

4.3. Estimation of the flame-induced pressure

This section presents our approach to determine the pressure field induced by the flame. The DNG-4000 flame was used to illustrate the approach.

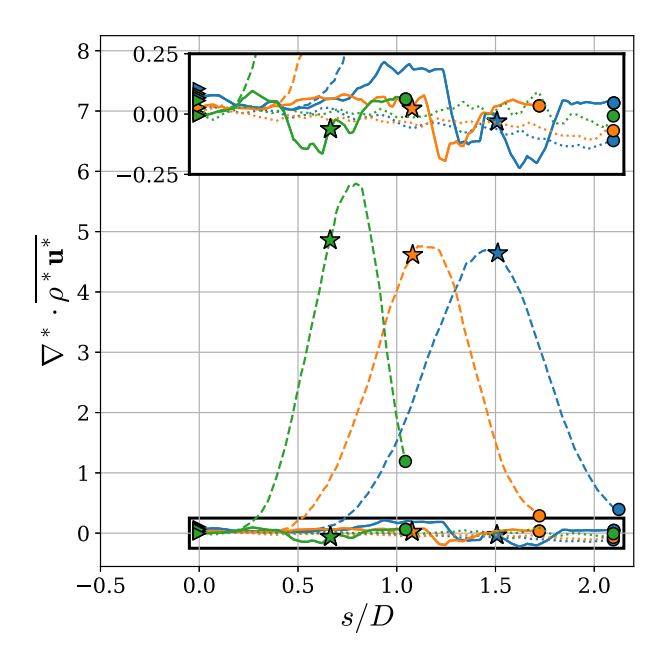


Fig. 14. The mass flux divergence along streamline path s(r, x) for three streamlines in reacting (solid and dashed lines) and non-reacting (dotted line) flow. The Favreaveraged and Reynolds-averaged approach are indicated by solid and dashed lines, respectively. The colors correspond to the colors of the streamlines in Fig. 13. The triangle and spheres correspond to the start and the end point of the corresponding streamline, respectively. The stars mark the intersection of the flame cone and the corresponding streamline.

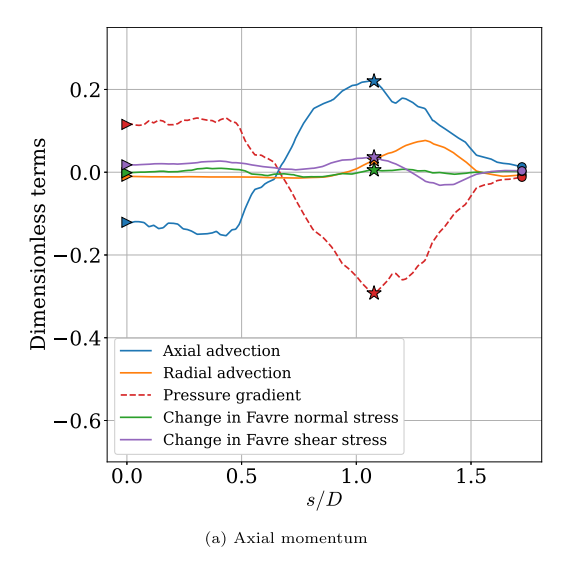
4.3.1. Mass conservation along streamlines

Fig. 13 shows three streamlines along which the pressure was determined for both the reacting and non-reacting flow. These streamlines, starting at radial locations r/D=0.1, r/D=0.2 and r/D=0.3 at a distance of x/D=0.1 above the burner exit, are radially deflected in the reacting flow and remain straight in the non-reacting flow. To determine the pressure along the streamlines, it is necessary to determine the pressure gradient terms in the Favre-averaged Navier-Stokes equations given in Section 2.1.

Fig. 14 shows the mass flux divergence $\nabla^* \cdot \overline{\rho^* \mathbf{u}^*}$ (see Eq. (1)) along streamline path s(r,x) for the three streamlines in both reacting and non-reacting flow. In the reacting flow, the mass flux divergence is represented by a solid line for the Favre-averaged approach and a dashed line for the Reynolds-averaged approach, where density is assumed to be constant throughout the flow field. The mass flux divergence along the streamlines for the non-reacting flow is indicated with dotted lines. In this figure, the mass flux divergence values for the Reynolds-averaged approach, indicated by dashed lines, strongly deviate from zero, showing that mass conservation is not achieved with this approach. In contrast, for both the non-reacting flow, indicated with dotted lines, and the Favre-averaged approach, indicated by solid lines, the mass flux divergence is almost zero. The observed minor deviations from zero are likely due to experimental inaccuracies.

4.3.2. Adverse pressure gradient calculation

Now that mass conservation along the streamlines is confirmed when using Favre-averaged quantities, it is possible to determine the (dimensionless) pressure gradient terms $\partial \overline{p^*}/\partial r^*$ and $\partial \overline{p^*}/\partial x^*$ in the Favre-averaged Navier-Stokes equations by computing all other terms in Eqs. (3) and (4) using a second-order accurate central difference scheme. The different terms in Eqs. (3) and (4) are plotted in Fig. 15 for the orange streamline in the reacting flow (see Fig. 13). It is seen in Fig. 15(a) that the positive pressure gradient is mainly balanced by the axial advection term in the axial momentum equation. A negative axial advection term indicates that the flow is decelerating. Following



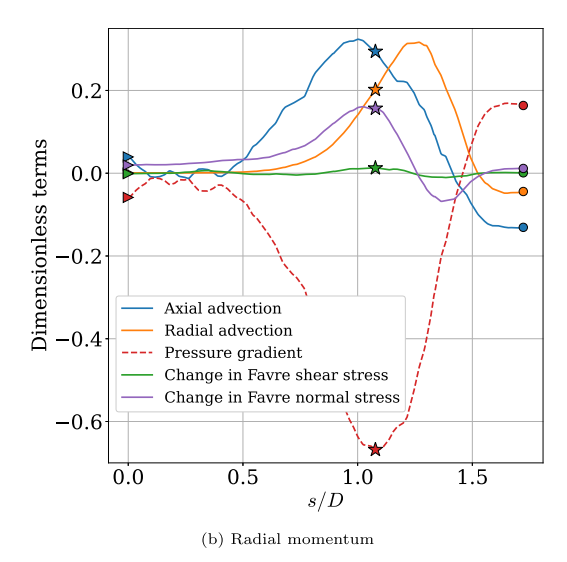
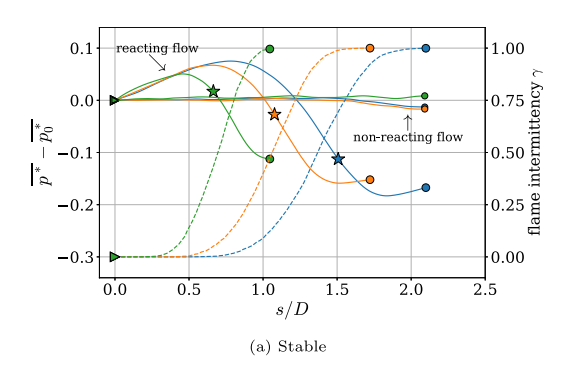


Fig. 15. Terms in the Favre-averaged Navier-Stokes equation in (a) axial direction, Eq. (3), and (b) radial direction, Eq. (4), along the orange streamline displayed in Fig. 13 for the DNG-4000 flame. The stars mark the intersection of the streamline and the flame cone.



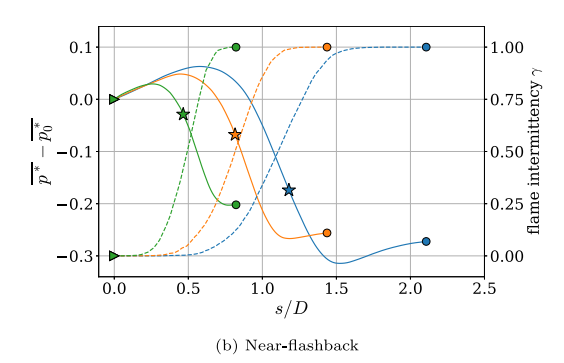


Fig. 16. Pressure (solid lines) and flame intermittency (dashed lines) along the three streamlines for the DNG-air flames with (a) DNG-4000 and (b) DNG-3000. The stars mark the intersection of the flame cone and the corresponding streamline.

the orange streamline it is seen that the flow decelerates up to a path length of $s/D \approx 0.6$, before an acceleration sets in with a maximum acceleration at the time-averaged location of the flame front, which is represented by the flame cone. Furthermore, Fig. 15(b) indicates a strong negative pressure gradient in radial direction, which is consistent with the radial deflection (curvature) of the streamlines in Fig. 13.

The dimensionless pressure \overline{p}^* along the streamline s(r,x) was then computed by integrating the contributions of the dimensionless pressure gradients in the radial direction and axial direction as:

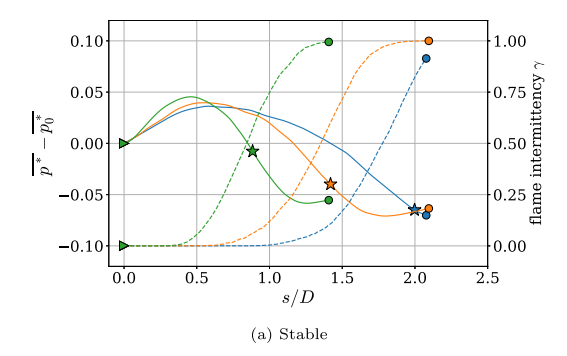
$$\overline{p^*} - \overline{p_0^*} = \int \frac{\partial \overline{p^*}}{\partial s^*} ds^* = \int \frac{\partial \overline{p^*}}{\partial r^*} dr^* + \int \frac{\partial \overline{p^*}}{\partial x^*} dx^*.$$
 (11)

In this equation the reference pressure $\overline{p_0^*}$ corresponds to the pressure at the start of the streamline and the dimensionless streamline path s^* is defined as $s^* = s(r,x)/D$. The computed (dimensionless) pressures along the three streamlines in the DNG-air flames and H_2 -air flames are shown in Figs. 16 and 17, respectively. Both figures show an initial increase in pressure when moving along the streamlines towards the time-averaged location of the flame front. This pressure increase is the back pressure induced by the flame. It is seen that the initial adverse pressure gradient in the hydrogen-air flame is largest for the streamline at r/D=0.3, while the initial adverse pressure gradient in the DNG-flames are practically the same for all three streamlines.

Fig. 16(a) also shows the computed pressure along the three streamlines in the non-reacting flow where, in contrast to the reacting flow, the pressure is seen to be nearly constant. Figs. 16 and 17 indicate a larger pressure drop over the mean flame front for the near-flashback flames compared to the stable flames, in both the DNG-air and the $\rm H_2$ -air flames. This observation is consistent with Fig. 9, where the near-flashback flames exhibit a higher velocity increase over the mean flame front. Figs. 16 and 17 also indicate that the pressure drop in the stable (near-flashback) DNG-air flame is higher than that in the stable (near-flashback) $\rm H_2$ -air flame. This is due to the higher expansion ratio of the stoichiometric DNG-air flames compared to the lean $\rm H_2$ -air flames.

In addition to pressure, Figs. 16 and 17 also show the value of the flame intermittency γ (that was introduced in Section 2.2) along the streamlines. In the DNG-air flames it is seen that the pressure steadily increases along the streamlines in the regions where $\gamma = 0$ (reactants only). The pressure reaches a maximum at (or very near) the location where the flame intermittency starts to increase above zero. In the H₂air flames the same behavior is observed for the streamline farthest from the centerline (at r/D = 0.3), but for the other streamlines (at r/D = 0.2 and r/D = 0.1) the maximum pressure occurs some distance before the flame intermittency starts to increase. A possible explanation is that when the intermittency increases above zero along a streamline with larger radius, such as r/D = 0.3, the pressure maximum also reached at smaller radii, suggesting that the flame-induced pressure field is not solely determined by local conditions. For all four flames considered it is observed that the pressure along the streamline increases again in the regions where the flame intermittency is equal to one (products only, $\gamma = 1$).

For both the DNG-air and H₂-air flames, it could be argued that the contrasting cases (stable vs. near-flashback) show only small differences



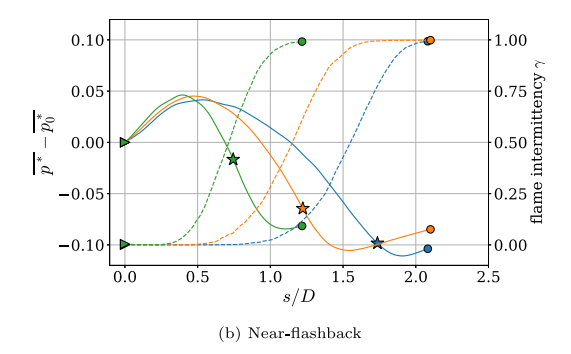
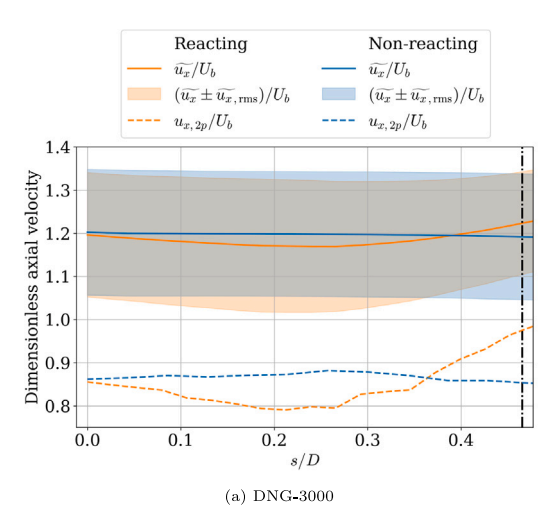


Fig. 17. Pressure (solid lines) and flame intermittency (dashed lines) along the three streamlines for the H_2 -air flames with (a) H_2 -16000 and (b) H_2 -12500. The stars mark the intersection of the flame cone and the corresponding streamline.



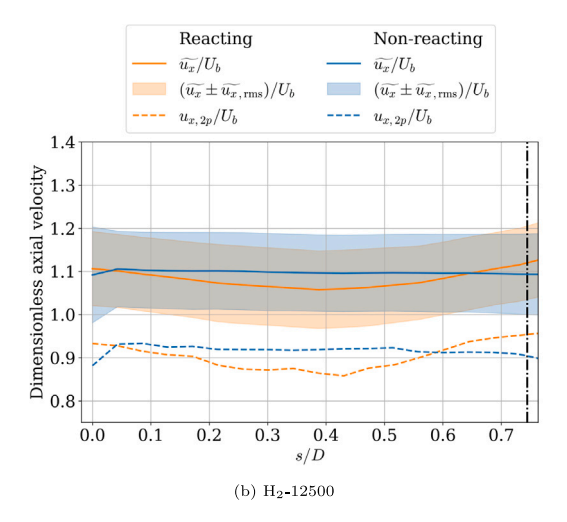


Fig. 18. The dimensionless Favre-averaged axial velocity $\widetilde{u_x}/U_b$, the root-mean-square of the dimensionless turbulent velocity fluctuations in axial direction $\widetilde{u_{x,rms}}/U_b$ and the second percentile dimensionless axial velocity $u_{x,2p}/U_b$ along the green streamline (starting at r/D=0.3) for the near-flashback flames (a) DNG-3000 and (b) H₂-12500. The black dashed line indicates the average flame front location.

in pressure profiles. Therefore, the pressure gradient is unlikely to play a significant role in flashback and does not serve as a reliable predictive metric. However, it may be valuable to analyze the flow retardation caused by the adverse pressure gradients and to compare the lowest velocities for the reacting and non-reacting flows for both the DNG-air and H₂-air flame. Fig. 18 shows the axial mean velocity along the streamline farthest away from the centerline (at r/D = 0.3) for the near-flashback cases of both the DNG-air (Fig. 18(a)) and the H₂-air flame (Fig. 18(b)). The figure presents the dimensionless Favre-averaged axial velocity $\tilde{u_x}/U_b$ along with the dimensionless rootmean-square of the turbulent velocity fluctuations in axial direction, $\widetilde{u_{x,\mathrm{rms}}}/U_b$, where the value of $\widetilde{u_{x,\mathrm{rms}}}$ is also calculated as a Favreaverage, i.e., $\widetilde{u_{x,\mathrm{rms}}} = \sqrt{(\widetilde{u_x''^2})}$. Also shown is the dimensionless value of the second percentile axial velocity $u_{x,2p}/U_b$, which is used here as a measure for the lowest axial velocities in the local axial velocity pdf. The results indicate a higher turbulence intensity for DNG-air flames compared to the H₂-air flames, which can be attributed to the fact that a higher Reynolds number, results in a lower turbulence intensity in pipe flow [28]. Another interesting observation from comparing the reacting and non-reacting flows is that the flow deceleration induced by the adverse pressure gradient primarily affects the mean flow velocity, while having minimal influence on the velocity fluctuations $\widetilde{u_{x,\mathrm{rms}}}$. Furthermore, by examining the profile of $\widetilde{u_x}/U_b$, a somewhat larger mean flow deceleration compared to the non-reacting flow is observed for the H₂-air flame compared to the DNG-air flame. When comparing the near-flashback cases (Fig. 18) to the stable cases (Fig. 19), it is seen that the decrease of the Reynolds number (bulk velocity) has very little effect on $\widetilde{u_x}/U_b$ and $\widetilde{u_{x,rms}}/U_b$ in both the DNG-air and H₂-air flames.

However, in the DNG-air flames, the dimensionless second percentile axial velocity, $u_{x,2p}/U_b$, significantly decreases with Reynolds number (bulk velocity). The adverse pressure gradient results in a decrease of especially the lowest velocities, which makes the DNG-air flame at low Reynolds numbers more prone to flashback. For the ${\rm H_2}$ -air flames, the dimensionless second percentile axial velocity, $u_{x,2p}/U_b$, at low Reynolds numbers is also below that of the high Reynolds number case, but the differences are smaller than those observed in the DNG-air flames. The reduction of the lowest velocities brings the flame closer to flashback, where a local flame front moves upstream into a low-velocity region issuing from the pipe.

The minimal differences in the time-averaged pressure gradients, flame front angle distributions and axial velocity percentiles between stable and near-flashback flames support the interpretation of flame flashback as a statistical phenomenon in the sense that it may occur at any moment when a local flame front moving upstream coincides with a patch of low velocity fluid moving downstream near the burner tube exit, with the probability of an occurrence of flashback gradually increasing with decreasing bulk velocity.

4.3.3. Cause of the adverse pressure gradient

The cause of the initial pressure increase when moving towards the flame front in Figs. 16 and 17 can be traced back to the Miescattering images and their corresponding instantaneous velocity fields shown in Figs. 20 and 21 for the near-flashback flames (DNG-3000 and $\rm H_2\text{-}12500$). In Fig. 20(a) an upstream propagating flame bulge is observed with the red line marking the flame front at time t_0 and the green line marking the flame front 0.5 ms later. The low velocity region

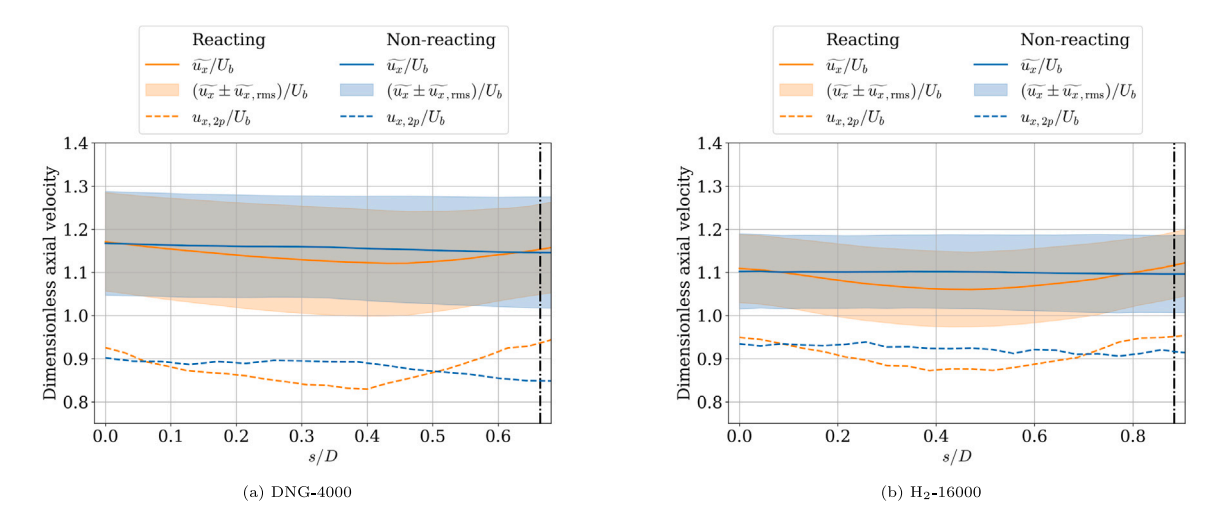


Fig. 19. The dimensionless Favre-averaged axial velocity $\widetilde{u_x}/U_b$, the root-mean-square of the dimensionless turbulent velocity fluctuations in axial direction $\widetilde{u_{x,rms}}/U_b$ and the second percentile dimensionless axial velocity $u_{x,2p}/U_b$ along the green streamline (starting at r/D=0.3) for the stable flames (a) DNG-4000 and (b) H₂-16000. The black dashed line indicates the average flame front location.

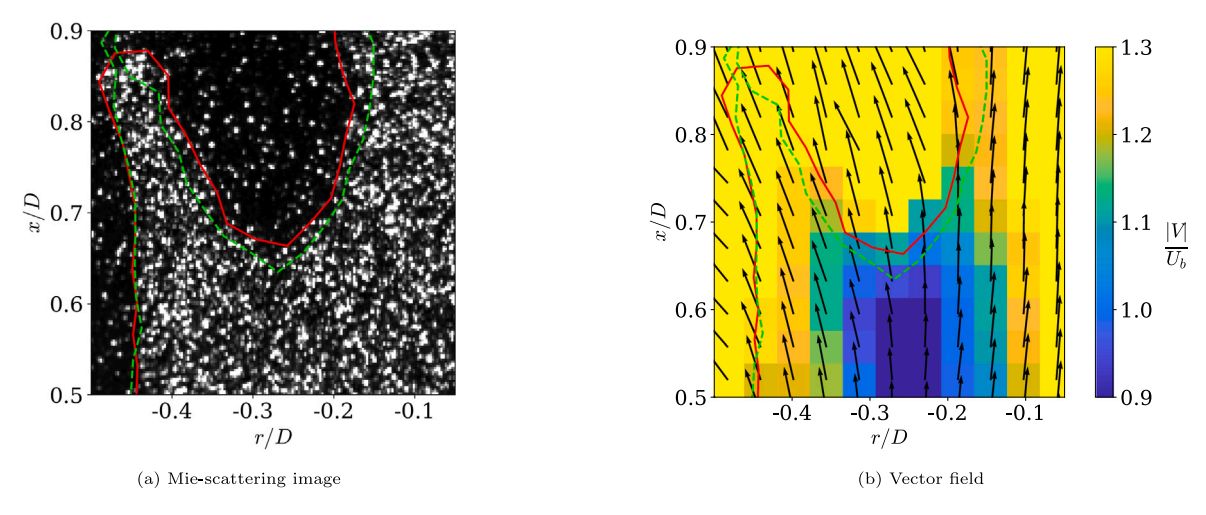


Fig. 20. (a) Mie-scattering image for the near-flashback stoichiometric DNG-air flame (DNG-3000) at time instant t_0 . The red solid line represents the instantaneous flame front at time t_0 ; the green dashed line represents the instantaneous flame front at time $t_1 = t_0 + 0.5 \,\text{ms}$. (b) The corresponding instantaneous velocity field with a low velocity region just in front of the upstream propagating flame front.

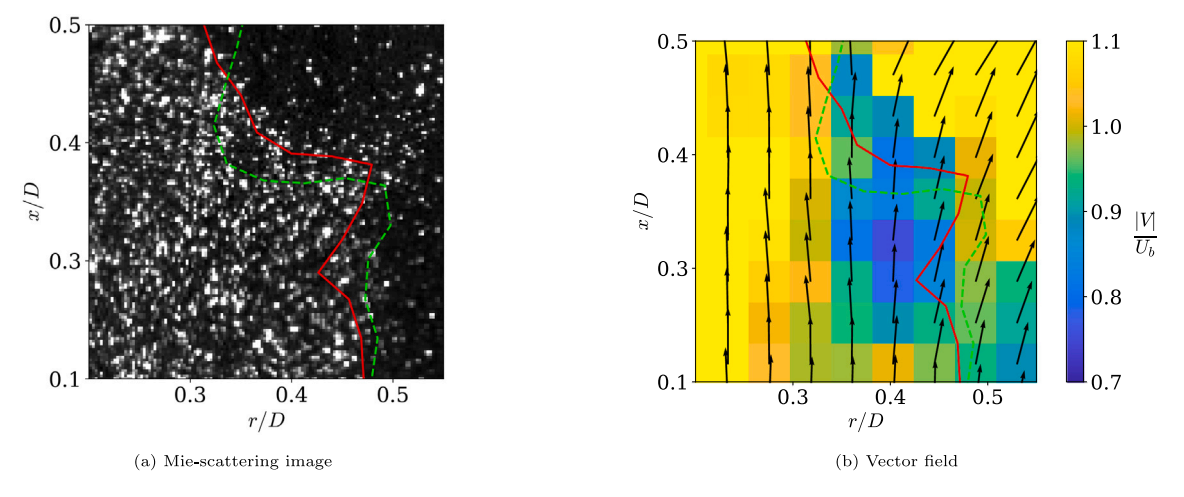


Fig. 21. (a) Mie-scattering image for the near-flashback lean H_2 -air flame (H_2 -12500) at time instant t_0 . The red solid line represents the instantaneous flame front at time t_0 ; the green dashed line represents the instantaneous flame front at time $t_1 = t_0 + 0.48$ ms. (b) The corresponding instantaneous velocity field with a low velocity region just in front of the upstream propagating flame front.

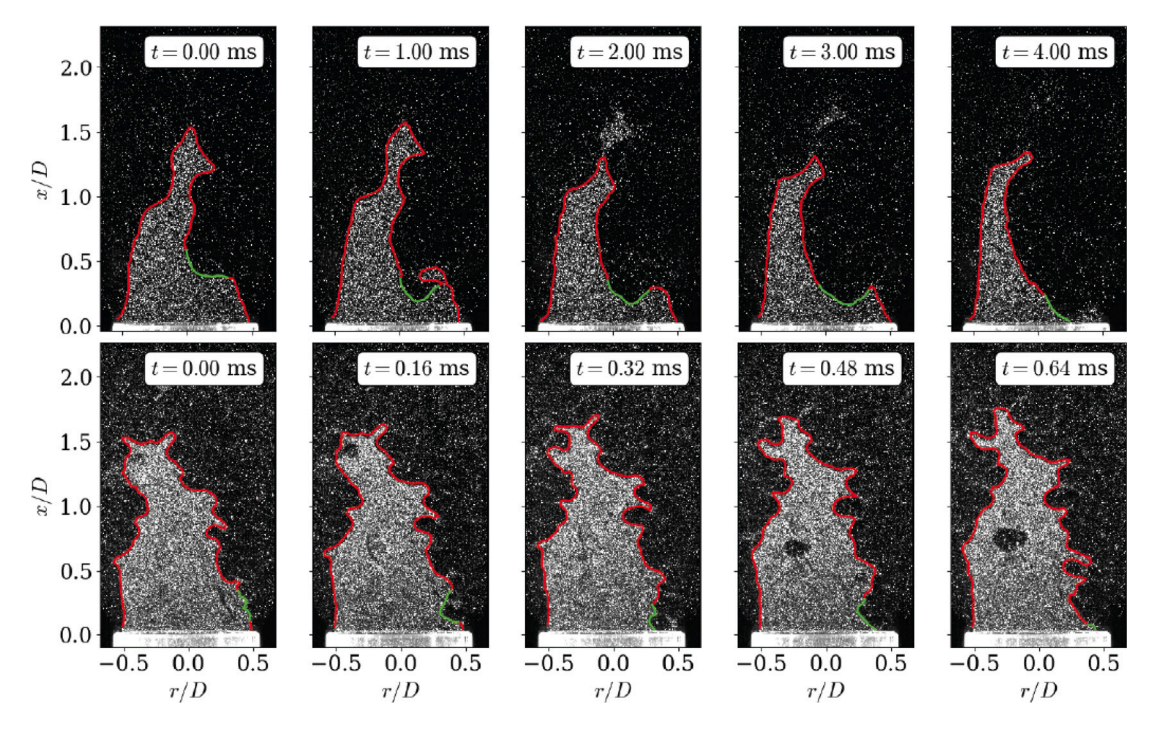


Fig. 22. A sequence of images capturing a flashback event of the DNG-air flame (top row) and the H_2 -air flame (bottom row), with both flashback events occurring on the right-hand side. The position of the upstream propagating flame bulge is highlighted in green. The flashback was initiated by a gradual lowering of the Reynolds number (bulk velocity) until flashback occurred at $Re_{D,fb} = 2700$ for the DNG-air flame and $Re_{D,fb} = 11900$ for the H_2 -air flame.

with the slightly diverging velocity field in Fig. 20(b) is indicative of a pressure increase in the fuel-air mixture flowing towards the upstream propagating flame front. Across the flame front there is a sudden increase in velocity accompanied by a decrease in density and pressure. Similar observations were made in the near-flashback H2air flame shown in Fig. 21. It is observed that the H₂-air flames are characterized by stronger flame front wrinkling and smaller bulge sizes compared to the DNG-air flames. The bulges displayed in Figs. 20 and 21 are relevant in understanding flame flashback, as these types of bulges are at the root of the phenomenon. This can be seen in Fig. 22, which shows two flashback events for the DNG-air flame (top row) and the H2-air flame (bottom row). In both flames, the flashback was initiated by a gradual lowering of the Reynolds number (bulk velocity) until flashback occurred at $Re_{D.f.h} = 2700$ for the DNG-air flame and $Re_{D,fb} = 11900$ for the H₂-air flame. In both cases, flashback occurs when a bulge, highlighted in green, propagates upstream and ultimately enters the quartz tube, resulting in flashback. The time intervals between the images indicate that the flashback of the H2-air flame occurs an order of magnitude faster compared to the DNG-air

A pressure increase ahead of the flame front and the accompanying low velocity region are also found in confined flows along solid walls in both experiments [9,11,13] and numerical simulations [15,29]. In confined flows it is possible that the pressure rise ahead of the flame front results in local flow reversal [11]. This was not observed in the jet flames considered in the present study.

5. Discussion and conclusion

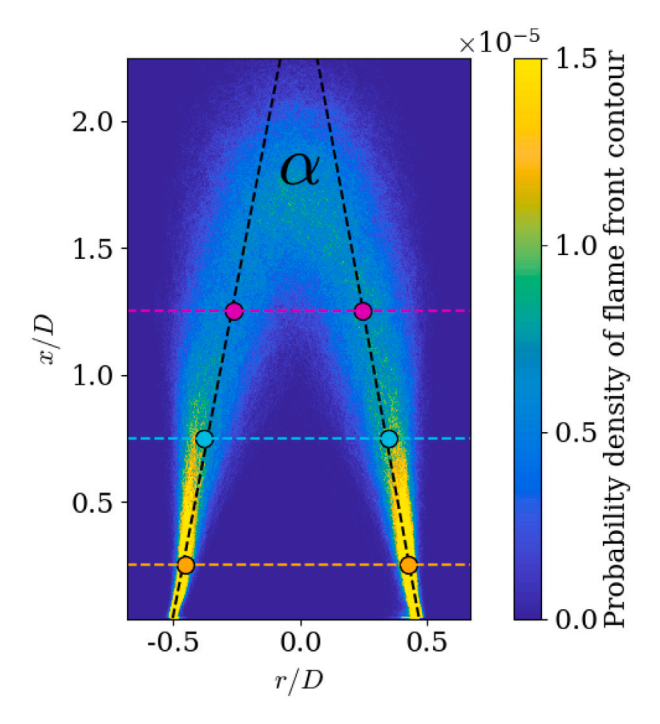
The flashback behavior of both premixed hydrogen-air and natural gas-air jet flames has been analyzed using different methodologies in the present study. A phenomenological assessment was conducted using the study of a flashback event. The flashback phenomenon for hydrogen and natural gas look quite similar (see Fig. 22): a flame bulge propagates upstream, and if it reaches the burner tube exit, it might cause a flashback, leading to flame propagation inside the burner. The comparison of the flame front orientation for a flame near-flashback

and a stable flame shows a systematic shift, with the flame front nearflashback oriented more perpendicular to the bulk flow direction (Fig. 11). The (instantaneous) adverse pressure created by the flame front (Fig. 20 for natural gas and Fig. 21 for hydrogen) perpendicular to the incoming flow results in a retardation of the velocity upstream of the flame front, facilitating the upstream propagation of a flame bulge.

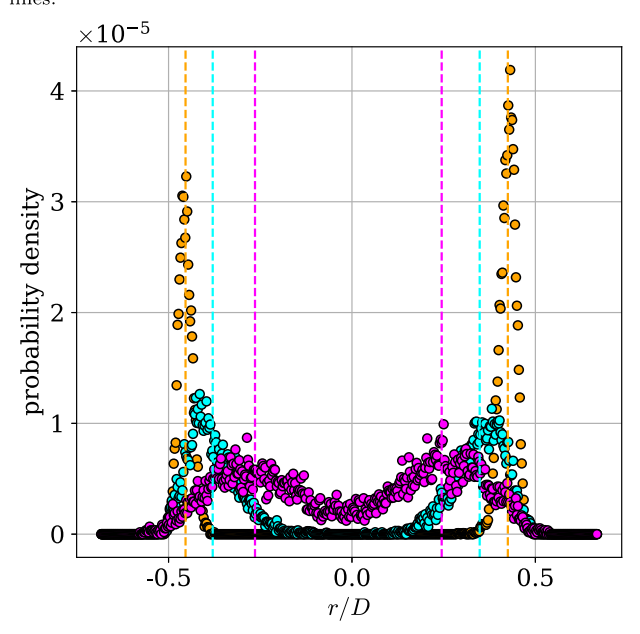
To better understand the impact of the flame-induced adverse pressure gradient on the flame behavior, a new method was developed to calculate the mean pressure gradient along the streamlines based upon PIV data only. For this method, the Reynolds-averaged density field must be known, which is derived from instantaneous Mie-scattering images using a new flame front detection method. The experimentally determined mean pressure gradients show only subtle differences between the stable flame and the near-flashback flame. Other time-averaged quantities, such as the pdf of the local flame front angle (Fig. 11) or the second percentile of the axial velocity (Figs. 18 and 19) also indicate only mild differences between the stable flame and the near-flashback flame, suggesting that these time-averaged quantities cannot be used as a predictor for the occurrence of flashback.

The methodology for the calculation of the Reynolds-averaged density field and the pressure gradient also enables the calculation of other Favre-averaged quantities like the turbulent kinetic energy. The comparison of the Reynolds-averaged (k) and Favre-averaged (\widetilde{k}) version of the turbulent kinetic energy show large differences, especially at the locations with flame intermittency. At these locations, a significant part of the (apparent) velocity fluctuations are a direct result of density fluctuations. These effect should be taken into account when comparing (turbulent) velocity fluctuation from experiments with those from numerical simulations.

The results from the flashback map (Fig. 8) show that there is a non-linear increase of the bulk velocity at flashback, $U_{b,fb}$, with the hydrogen content in the fuel. As discussed above the basic phenomenon for flashback is similar for hydrogen and natural gas. There is a large difference in the flashback limit of the considered DNG-air flames ($U_{b,fb}/S_{L0}\approx 5$) and the hydrogen-air flames ($U_{b,fb}/S_{L0}\approx 24$). This difference is speculated to result from nonequidiffusion effects in the hydrogen-air flame (with Lewis number Le=0.43 and fuel-to-oxidizer



(a) Probability density of the flame front contour for DNG-4000. The colored circle markers indicate the flame front location resulting from Figure A.23b. The black dashed lines indicate the average flame front estimated using a first order fit through the colored points. The flame cone angle α is derived from these black dashed lines



(b) Probability density of the flame front contour at three axial locations: x/D=0.25 (red), x/D=0.75 (cyan) and x/D=1.00 (orange). The vertical dashed lines correspond to the average radial location of the flame front. These radial location correspond with the circle markers in Figure A.23a.

Fig. A.23. Overview of the cone angle determination: (a) PDF of the flame front contour for the entire image and (b) at three axial locations.

diffusion ratio ($D_f/D_{\rm O_2}=3.74$) and the absence of these effects in the natural gas-air flame (with Le=1.02 and $D_f/D_{\rm O_2}=1.06$). The structure of the resulting flame bulges associated with this effect can e.g. be seen in the instantaneous Mie-scattering images (Fig. 22).

CRediT authorship contribution statement

Luuk A. Altenburg: Writing – original draft, Methodology, Investigation, Formal analysis, Conceptualization. **Sikke A. Klein:** Writing – review & editing, Supervision, Project administration, Funding acquisition, Conceptualization. **Mark J. Tummers:** Writing – review & editing, Supervision, Methodology, Conceptualization.

Declaration of competing interest

The authors declare that they have no known competing financial interests or personal relationships that could have appeared to influence the work reported in this paper.

Acknowledgments

This work was partly funded by Rijksdienst voor Ondernemend Nederland (RVO), The Netherlands under project DEI120081: High Hydrogen Gas Turbine Combustor High Pressure Test.

Appendix. Cone angle determination

The cone angle α was calculated from the probability density of the instantaneous flame fronts, which were determined using the method described in Section 2.3. Fig. A.23(a) shows the probability density of the flame front for the DNG-4000 case. To find the cone angle, two average radial locations of the flame front were determined at three axial locations, i.e. x/D=0.25, x/D=0.75, and x/D=1.25, see Fig. A.23(b). The average radial location corresponds to the mean of the distribution on left and right side of the flame front, which was divided at r/D=0. Subsequently, straight lines were fitted to the left and right average flame front coordinates. Finally, the cone angle α was calculated from the slopes of these fitted lines.

References

- [1] T. Lieuwen, V. McDonell, D. Santavicca, T. Sattelmayer, Burner development and operability issues associated with steady flowing syngas fired combustors, Combust. Sci. Technol. 180 (6) (2008) 1169–1192.
- [2] C.K. Law, Combustion Physics, Cambridge University Press, 2010.
- [3] A. Kalantari, V. McDonell, Boundary layer flashback of non-swirling premixed flames: Mechanisms, fundamental research, and recent advances, Prog. Energy Combust. Sci. 61 (2017) 249–292.
- [4] B. Lewis, G. von Elbe, Stability and structure of burner flames, J. Chem. Phys. 11 (2) (1943) 75–97.
- [5] G. Von Elbe, M. Mentser, Further studies of the structure and stability of burner flames, J. Chem. Phys. 13 (2) (1945) 89–100.
- [6] L.E. Bollinger, R. Edse, Effect of burner-tip temperature on flash back of turbulent hydrogen-oxygen flames, Ind. Eng. Chem. 48 (4) (1956) 802–807.
- [7] L.N. Khitrin, P.B. Moin, D.B. Smirnov, V.U. Shevchuk, Peculiarities of laminarand turbulent-flame flashbacks, in: Symposium (International) on Combustion, vol. 10, (1) 1965, pp. 1285–1291.
- [8] C. Eichler, T. Sattelmayer, Experiments on flame flashback in a Quasi-2D turbulent wall boundary layer for premixed methane-hydrogen-air mixtures, J. Eng. Gas Turbines Power 133 (1) (2011) 011503.
- [9] C. Eichler, G. Baumgartner, T. Sattelmayer, Experimental investigation of turbulent boundary layer flashback limits for premixed hydrogen-air flames confined in Ducts. J. Eng. Gas Turbines Power 134 (1) (2012) 011502.
- [10] Z. Duan, B. Shaffer, V. McDonell, G. Baumgartner, T. Sattelmayer, Influence of burner material, tip temperature, and geometrical flame configuration on flashback propensity of H2-air jet flames, J. Eng. Gas Turbines Power 136 (2) (2014) 021502.
- [11] C. Heeger, R.L. Gordon, M.J. Tummers, T. Sattelmayer, A. Dreizler, Experimental analysis of flashback in lean premixed swirling flames: upstream flame propagation, Exp. Fluids 49 (4) (2010) 853–863.
- [12] C. Eichler, T. Sattelmayer, Premixed flame flashback in wall boundary layers studied by long-distance micro-PIV, Exp. Fluids 52 (2) (2012) 347–360.
- [13] D. Ebi, N.T. Clemens, Experimental investigation of upstream flame propagation during boundary layer flashback of swirl flames, Combust. Flame 168 (2016) 39–52.
- [14] D. Ebi, R. Ranjan, N.T. Clemens, Coupling between premixed flame propagation and swirl flow during boundary layer flashback, Exp. Fluids 59 (7) (2018) 1–16.

- [15] A. Gruber, J.H. Chen, D. Valiev, C.K. Law, Direct numerical simulation of premixed flame boundary layer flashback in turbulent channel flow, J. Fluid Mech. 709 (2012) 516–542.
- [16] G. Baumgartner, L.R. Boeck, T. Sattelmayer, Experimental investigation of the transition mechanism from stable flame to flashback in a generic premixed combustion system with high-speed micro-particle image velocimetry and micro-PLIF combined with chemiluminescence imaging, J. Eng. Gas Turbines Power 138 (2) (2016) 021501.
- [17] G. Chen, H.O. Wang, A. Gruber, K. Luo, J.R. Fan, Study of flame-flow interactions in turbulent boundary layer premixed flame flashback over a flat plate using direct numerical simulation, J. Fluid Mech. 971 (2023) A19.
- [18] Z.F. Zhu, H.O. Wang, G. Chen, K. Luo, J.R. Fan, Interactions of turbulence and flame during turbulent boundary layer premixed flame flashback under isothermal and adiabatic wall conditions using direct numerical simulation, Phys. Fluids 35 (12) (2023) 125106.
- [19] A.W. Vreman, J.A. van Oijen, L.P.H. de Goey, R.J.M. Bastiaans, Direct numerical simulation of hydrogen addition in turbulent premixed bunsen flames using flamelet-generated manifold reduction, Int. J. Hydrog. Energy 34 (6) (2009) 2778–2788
- [20] F. Faldella, S. Eisenring, T. Kim, U. Doll, P. Jansohn, Turbulent flame speed and flame characteristics of lean premixed H2-CH4 flames at moderate pressure levels, J. Eng. Gas Turbines Power- Trans. Asme 146 (2) (2024) 1–32.

- [21] S. Pfadler, F. Beyrau, A. Leipertz, Flame front detection and characterization using conditioned particle image velocimetry (CPIV), Opt. Express 15 (23) (2007) 15444.
- [22] Y. Zheng, L. Weller, S. Hochgreb, Instantaneous flame front identification by mie scattering vs. OH PLIF in low turbulence bunsen flame, Exp. Fluids 63 (5) (2022).
- [23] C. Tomasi, R. Manduchi, Bilateral filtering for gray and color images, in: Sixth International Conference on Computer Vision (IEEE Cat. No. 98CH36271), IEEE, 1998, pp. 839–846.
- [24] E. Oldenhof, M.J. Tummers, E.H. van Veen, D.J.E.M. Roekaerts, Ignition kernel formation and lift-off behaviour of jet-in-hot-coflow flames, Combust. Flame 157 (6) (2010) 1167–1178.
- [25] C.R. Wilke, A viscosity equation for gas mixtures, J. Chem. Phys. 18 (4) (1950) 517-519
- [26] G.P. Smith, D.M. Golden, M. Frenklach, N.W. Moriarty, B. Eiteneer, M. Goldenberg, C.T. Bowman, R.K. Hanson, S. Song, W.C. Gardiner, V.V. Lissianski, Z. Oin, GRI-mech 3.0, 2006.
- [27] S.P.R. Muppala, M. Nakahara, N.K. Aluri, H. Kido, J.X. Wen, M.V. Papalexandris, Experimental and analytical investigation of the turbulent burning velocity of two-component fuel mixtures of hydrogen, methane and propane, Int. J. Hydrog. Energy 34 (22) (2009) 9258–9265.
- [28] H. Fellouah, C.G. Ball, A. Pollard, Reynolds number effects within the development region of a turbulent round free jet, Int. J. Heat Mass Transfer 52 (17–18) (2009) 3943–3954.
- [29] A. Endres, T. Sattelmayer, Numerical investigation of pressure influence on the confined turbulent boundary layer flashback process, Fluids 4 (3) (2019) 146.